Power optimization and effective stiffness for a vibration energy harvester with displacement constraints

Binh Duc Truong, Cuong Phu Le & Einar Halvorsen

University College of Southeast Norway

Accepted version of article in
Journal of Micromechanics and Microengineering. 2016, 26 (12), 1-9.

Power optimization and effective stiffness for a vibration energy harvester with displacement constraints

Binh Duc Truong, Cuong Phu Le and Einar Halvorsen

Department of Micro- and Nanosystem Technology, University College of Southeast Norway, Campus Vestfold, Raveien 215, 3184 Borre, Norway

E-mail: Einar.Halvorsen@hbv.no

Abstract. This paper presents experiments on how to approach the physical limits on power from vibration energy harvesting under displacement-constrained operation. A MEMS electrostatic vibration energy harvester with voltage-control of the system stiffness is used for this purpose. The power saturation problem, when the proof-mass displacement reaches a maximum amplitude for sufficient acceleration amplitude, is shifted to higher accelerations by use of load optimization. In addition we demonstrate the effect of varying the electromechanical coupling k^2. Measurement results show that harvested power can be made to follow the optimal power of the velocity-damped generator also for a range of accelerations that implies displacement constraints. Comparing to the saturated power, the power increases 1.5 times with the optimal load for electromechanical coupling k^2=8.7%. The improvement is 2.3 times for a higher coupling of k^2=17.9%. The obtained system effectiveness exceeds 60%. This work shows a first demonstration of reaching optimal power in the intermediate acceleration-range between the two extremes of maximum efficiency and maximum power transfer. The experimental results follow the theoretical results for a device with both load and stiffness tuning surprisingly well despite only optimizing the load here. We compared a linearized lumped-model of the device with the same augmented by end-stop nonlinearities. The comparison shows that an effective stiffness due to end-stop impacts in the latter model closely matches the optimal stiffness for the former model and therefore can explain why the experimental output power is close to optimal despite lack of deliberate stiffness tuning.

1. Introduction

Microelectromechanical systems (MEMS) vibration energy harvesting (VEH) is a potential approach to autonomously supply power to wireless sensors. Potential applications are found in structural health monitoring [1, 2], automobiles and machinery [3, 4] as well as wearable or implantable sensors [5, 6]. A typical VEH design is a spring-mass system. The proof mass motion induced by ambient vibrations leads to energy conversion based on either of three basic mechanisms: piezoelectric, electromagnetic and electrostatic conversion [7–11]. Most vibration energy harvesters can be considered two-port harvesters with two coupled generalized displacements, one mechanical (the proof-mass displacement) and one electrical (an electrode charge) or magnetic (a flux linkage).

It is sometimes convenient to distinguish two different regimes of energy harvester operation. In one, the output power is limited by the available space for the proof mass to move in. We will

refer to this as displacement-constrained or displacement-limited operation. The other is when the optimal proof mass displacement is smaller than the physical constraints of the device so that the proof mass displacement is limited by the electrical damping due to energy conversion and parasitic mechanical damping. We will refer to this situation as damping-limited. Optimization of linear two-port devices for harmonic vibrations corresponds to maximizing power transfer and results in an efficiency of 1/2. For sufficiently low accelerations, one will always achieve damping-limited operation. For low-loss resonant harvesters at the micro-scale, displacement-constrained operation is also easily encountered at realistic accelerations because of the limited space available on chip and the desire for low mechanical loss.

Several devices using impact mechanisms [12–16] have shown usefulness for widening system bandwidth and for low-frequency vibrations such as human motion. However, beyond a critical acceleration sufficient to drive the proof mass displacement to its maximum amplitude, the output power saturates [12,17] and is left increasingly far below the theoretical power bound for displacement-limited operation [18]. This bound is conservatively approximated by the optimal velocity-damped generator (VDRG) whose power increases linearly with acceleration [19].

A pressing question is how to avoid saturation and further improve power for acceleration amplitudes beyond the critical value? Utilization of transducing end-stops in our previous impact-device concept [20] somewhat overcomes this problem, but it demands complex optimization of the device design to further increase power in the impact regime [21]. An approach using electric control is used to optimize the end-stop transducer performance and thereby further improve the system effectiveness when the displacement amplitude reaches its maximum limit [22].

For a linear two-port harvester under displacement-constrained operation it has been shown that it is ultimately optimal to maximize efficiency [23] which is equivalent to maximizing electrical damping. Hence, maximum efficiency and maximum power transfer (unconstrained motion) constitute two extremes, but the intermediate optimization cases have not been well studied.

In this paper, which is an extension of a previous conference contribution [24], we investigate an approach to optimize power in both damping-limited regime and displacement-limited regime. Harvester power is then maximized in the intermediate range. The approach is motivated by electrical damping being the control parameter in optimization of the VDRG [19]. We here consider load-resistance optimization and adjustment of the electromechanical coupling. Both these factors directly affect the electric damping and are used to keep the displacement amplitude at the limit for the VDRG.

It should be noted that a resistive load such as we use here can emulate a buck-boost converter that has no input filter capacitor [25]. It is therefore much more than an experimental convenience and can actually represent a rectifying circuit. The buck-boost circuit has an effective input resistance that is given by the duty cycle and the switching frequency. Hence, the resistance can be electrically controlled.

As an alternative circuit one might consider the standard diode bridge. It gives a comparable, but slightly lower, output power than the resistive load. This is the case both for unconstrained motion [25] and for displacement-constrained motion [26]. However, adding load tuning to the bridge circuit would lead back to buck-boost configurations of the type discussed in [25].

For the experiments, we employ a previous large-frequency-tuning-range resonator device [27] as a MEMS electrostatic vibration energy harvester. The system stiffness and the electromechanical coupling can be adjusted by an applied voltage. We use this capability to set two different values of stiffness, and therefore also electromechanical coupling factor. This is a means to generate two different experimental conditions and is an alternative to making two different devices. We use an electrically controllable load resistance to explore the optimization problem.

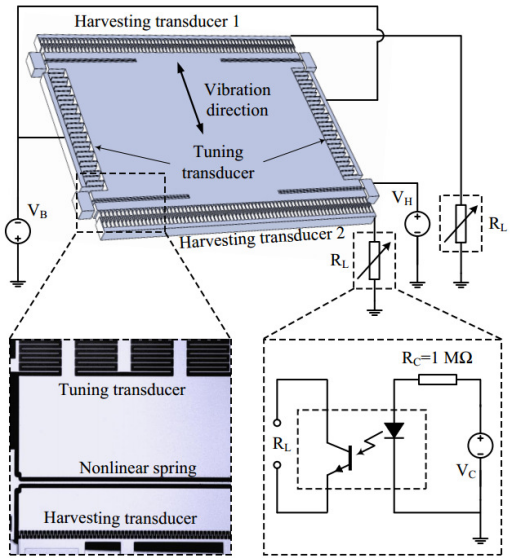

Figure 1: Key features of the device design, sketch of the electrical setup with the load tuning control. A close-up view of device fabricated using the SOIMUMPS process with the device layer thickness of $t = 25$ μm.

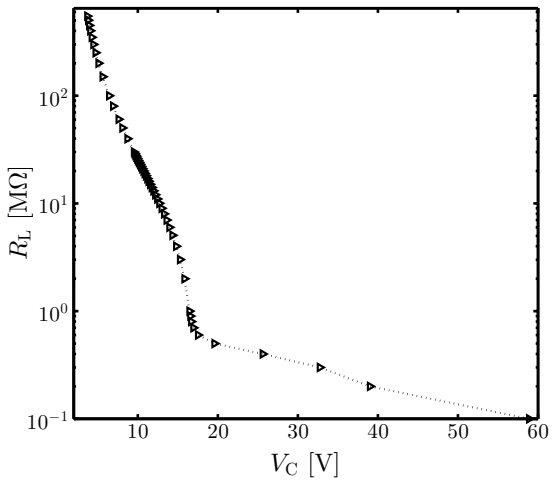

Figure 2: Characterization of the opto-coupling resistor under driving of the voltage source V_C.

2. MEMS device

Figure 1 shows key features of the electrostatic device. The harvesting transducers are two anti-phase comb-drive capacitor structures with a nominal capacitance C_0=0.47 pF. The proof mass is suspended by four single beams. The restoring force is designed to have a hardening nonlinearity. The device stiffness can be varied by a bias control V_T=V_H+V_B of an additional transducer which is a gap-closing capacitor structure. Increasing the bias shifts the harvester resonance to lower frequencies and simultaneously increases the electromechanical coupling. This feature is used to make the two cases of coupling referred to in the sections that follow. It is used as an alternative to designing two devices with different stiffness and coupling.

When the electrodes of the harvesting transducers are short-circuited, the net force on the

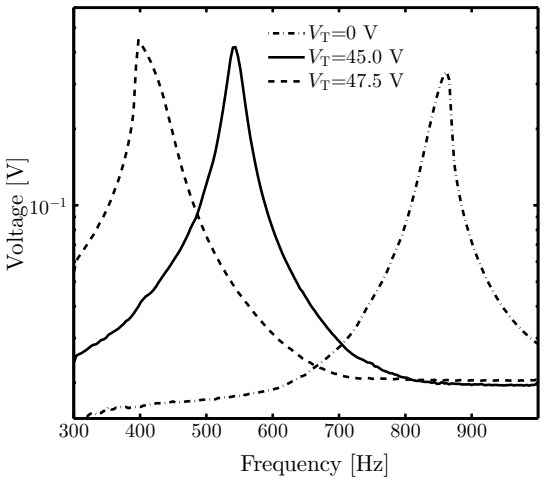

Figure 3: Measured frequency responses for increase of the control voltage V_T at a small acceleration A= 0.21 g and the load R_L=20 MΩ.

proof mass is approximately

$$F_{net}(x) = (k_m - \frac{C_T}{g^2}V_T^2)x + (\frac{k_m}{l^2} - \frac{2C_T}{g^4}V_T^2)x^3 \quad (1)$$

where k_m is the linear stiffness of the restoring force, l=$\sqrt{\frac{735}{512}}w$, w is the beam width, g and C_T are the nominal gap and the nominal capacitance of the additional transducer used for stiffness control. The generated power is obtained by connection of the fixed electrode of the harvesting transducers to the variable load R_L. To avoid cumbersome resistor changes, the load used in the experiment is the opto-coupling resistor V0617A with low coupling capacitance. The load value R_L is set by a voltage V_C and a series resistance R_C. This solution is convenient with respect to control, more repeatable than soldering resistors, and a more compact solution that is easier to shield than a switch box with resistors. Figure 1 also displays a close-up view of the device, which is fabricated using the SOIMUMPS process with a device layer thickness of t=25 μm. The nonlinear spring and a part of all transducers are shown in the optical micrograph. By design, the maximum amplitude of the proof mass displacement X_{max}=5.5 μm is defined by rigid end-stops. Further details of the device parameters can be found in [27].

3. Measurements

The opto-coupling resistor is characterized under control of the voltage V_C and a series resistance R_C=1 MΩ as shown in figure 2. The optical coupling between the diode emitter and the photo-transistor leads to a variable resistance that is high at low V_C and vice-versa. The load can be adjusted from 500 MΩ down to 100 kΩ when V_C varies from 3.7 V to 58.9 V. This characterization is used in all measurements of the device. The bias voltage for the harvesting transducers is chosen as V_H=45.0 V.

Figure 3 shows the measured frequency responses at small acceleration amplitudes when the proof mass displacement amplitude is still below the limit X_{max}. The hardening effect due to the nonlinear spring is evident for V_T=0.0 V with a center frequency 831.5 Hz. The effective stiffness of the system reduces with increase of the bias V_T, giving higher output voltages and lower center frequencies. The system response is roughly linear for V_T=45.0 V, which gives a center frequency f_c=531.5 Hz. The device exhibits softening effects for V_T=47.5 V. The critical voltage that causes pull-in instability is estimated to $V_{cr} \sim$ 50 V. We now use V_T = 45.0 V as

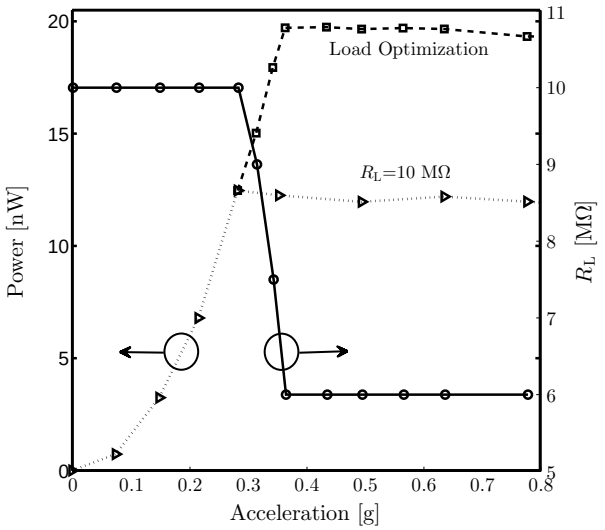

Figure 4: Measured power in damping-limited regime and displacement-limited regime with corresponding optimal load for V_T=45.0 V and the center frequency f_c=531.5 Hz.

a case for load optimization in both the damping-limited regime and the displacement-limited regime.

Figure 4 shows measured powers and corresponding optimal load for each RMS acceleration amplitude at the center frequency f_c. In the damping-limited regime, the optimal load is R_L=10 MΩ in this case. Keeping this resistance while varying the acceleration, the power saturates at P_c=12.4 nW for accelerations larger than a critical value A_c=0.28 g. We interpret this as the proof mass displacement reaching the maximum X_{max} at A_c and that it hits the end-stops for $A > A_c$. However, the power can be improved for $A > A_c$ by adjusting the load separately for every acceleration amplitude. The measured result shows that the power can be improved for acceleration amplitudes between A_c and 0.36 g where the power looks approximately linear in A. For $A > 0.36$ g the power saturates at 19.7 nW. All corresponding optimal loads and accelerations can be found in figure 4. The optimal load only varies between A_c and 0.36 g and is again constant for $A > 0.36$ g. Note that no attempt is made to avoid proof mass impacts on the end-stops. Therefore the power-acceleration curve here is significantly different from the theoretical result in [18] for large accelerations. It is reasonable to interpret the optimized value R_L=6.0 MΩ as the resistance value that gives maximum electrical damping.

The optimization of the power generated by a VDRG [19] provides a basis for interpreting our results. For unconstrained displacement at small acceleration amplitudes, the harvested power can be maximized by making the electrical damping equal to the mechanical damping. This is similar to the optimization in [28]. Due to the approximately linear behaviour, the optimal load is constant under these conditions. If the drive acceleration is large enough to drive the proof mass displacement to or beyond its maximum X_{max}, it is beneficial instead to increase the electrical damping in order keep the displacement at $X = X_{max}$ because the maximum output power is linearly proportional to the electrical damping at fixed displacement amplitude. As a consequence of reoptimizing the electrical damping, the output power can be further increased even though the maximum displacement is reached. The electrical damping is here increased by decreasing the load resistance. When the acceleration amplitude reaches $A \approx 0.36$ g, it is not possible to further increase the electrical damping by changing the load resistance, resulting in a saturated output power and a constant optimal load for further increase of the acceleration amplitude. For a linear device, we would expect a maximal electric damping at a load resistance

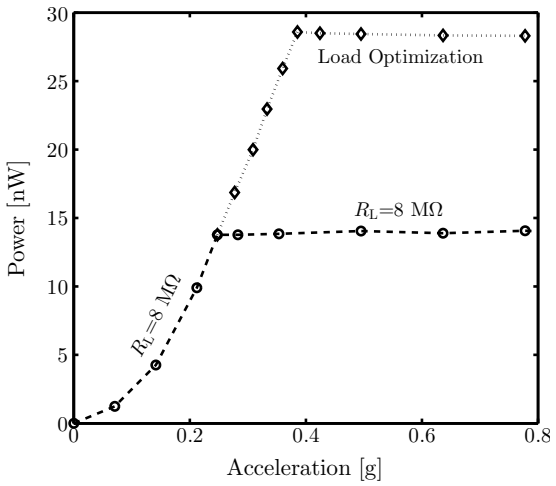

Figure 5: Measured power both with and without load optimization for V_T=47.5 V and the center frequency f_c=400.0 Hz.

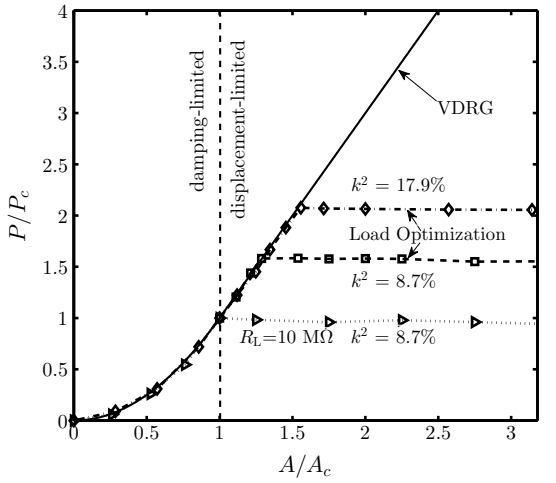

Figure 6: Comparison of the maximum power to the optimal velocity-damped generator VDRG for $k^2 = 8.7\%$ (V_T=45.0 V) and $k^2 = 17.9\%$ (V_T=47.5 V).

$1/\omega C$ where C is the transducer capactiance and ω is the angular frequency of the vibration.

Increase of the bias voltage V_T leads to a reduced net stiffness and higher electromechanical coupling k^2. This is advantageous with respect to further increase the harvested power under displacement-constrained operation. Figure 5 shows the measured power for V_T=47.5 V when driven at the center frequency f_c=400.0 Hz. The device now reaches a higher critical power of P_c=13.8 nW at a lower A_c=0.25 g, compared to the previous case of V_T=45.0 V. With load optimization for $A > A_c$, the power continues to increase to a maximum of 28.6 nW at A=0.38 g. This power is about 1.5 times better than the previous case.

In the linear approximation, the anti-phase comb-drive harvesting transducers are equivalently converted to a two-port model because of decoupling of the common and differential modes [29, 30]. For a displacement-limited linear two-port device, one can show that load optimization can boost the harvested power to a maximum value of

$$P_{\max} \approx \frac{1}{2} k^2 Q_m P_c \tag{2}$$

Table 1: Measured electromechanical coupling factor k^2 and figure of merit $M = k^2 Q_\mathrm{m}$ at A=0.03 g.

Bias voltage	k^2	$k^2 Q_\mathrm{m}$
V_T= 45.0 V	8.7%	3.2
V_T= 47.5 V	17.9%	4.7

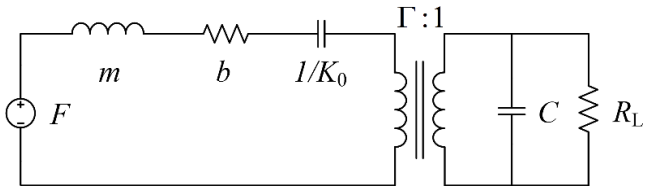

Figure 7: Linear two-port model.

where the mechanical quality factor Q_m is estimated from the full bandwidth at half maximum of the open-circuit frequency response and k^2 is the electromechanical coupling of the linear two-port model, evaluated by

$$k^2 = 1 - \frac{f_\mathrm{r}^2}{f_\mathrm{ar}^2} \tag{3}$$

where f_r is the resonant frequency measured with short-circuited output and f_ar is the resonant frequency measured with open-circuited output. Table 1 shows the measured coupling k^2 and a corresponding figure of merit $k^2 Q_\mathrm{m}$.

The achieved power is compared to the maximum possible power of the optimal velocity-damped generator under displacement-constrained operation in figure 6. The power and the acceleration are normalized by the factors P_c and A_c respectively because P/P_c is a universal function of A/A_c for all VDRGs. The comparison in the damping-limited regime shows that the power obtained with load optimization closely approaches the optimal VDRG up to a maximum acceleration beyond A_c. In the displacement-limited regime, the range of accelerations where the optimum can be followed depends on $k^2 Q_\mathrm{m}$ as is seen by comparing the maximum power $1.54 P_\mathrm{c}$ at $A = 1.28 A_\mathrm{c}$ for $k^2 = 8.7\%$ to the maximum power $2.07 P_\mathrm{c}$ at $A = 1.55 A_\mathrm{c}$ for $k^2 = 17.9\%$. The corresponding estimates of maximum power from (2) are respectively $1.6 P_\mathrm{c}$ and $2.4 P_\mathrm{c}$ giving best correspondence with the lowest-coupling configuration which is also the most linear one. It is noteworthy that even though the high-coupling configuration exhibited clear softening nonlinearities, it follows the optimal VDRG curve as closely as the other alternative until its maximum is reached.

4. Effective stiffness tuning by end-stops

The results in figure 6 that the ouput power closely follows the VDRG characteristic into the displacement limited regime before it saturates at a constant value of P/P_c is also seen in simulations of two-port harvesters with linear transducers and rigid end-stops [31]. Both are strongly reminiscent of a linear two-port harvester whose maximum displacement is limited by choice of stiffness and load and not by end-stops [32]. In that case the performance can be characterized by a figure of merit $M = \Gamma^2 / C\omega b \approx k^2 Q_\mathrm{m}$, in particular the maximum power is $P/P_\mathrm{c} = M/2$ which is reached at $A/A_\mathrm{c} = (1 + M/2)/2$. The normalized power and acceleration for M=3.2, are $P/P_\mathrm{c} = 1.60$ and $A/A_\mathrm{c} = 1.30$ while the corresponding values obtained in the experiment are 1.54 and 1.28 respectively. These comparisons suggest that the end-stops

Table 2: Model parameters

Parameters	**Value**
Proof mass, m	0.739 mg
Spring stiffness, k_{m}	22 N/m
Thin-film air damping, b	2.4e-5 Ns/m
Nominal capacitance, C_0	0.47 pF
Parasitic capacitance, C_{p}	7.50 pF
Load capacitance, C_{L}	8.6 pF
Nominal overlap, x_0	10 μm
Contact stiffness, k_{s}	3.4 MN/m

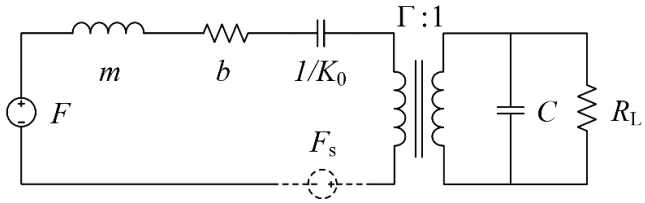

Figure 8: Two-port model including impact force.

contribute a stiffness-tuning with an effective stiffness that corresponds at least approximately to the optimal stiffness of a displacement-limited harvester without end-stops.

In order to test the hypothesis regarding the effect of end-stops on the vibration energy harvester performance, we compare a linearized lumped-model as in figure 7 and the same type of model with an end-stop force F_{s} added as in figure 8, where m - proof mass, b - damping constant, F - inertial force, C - capacitance and R_{L} - load resistance. We compare output power, stiffness parametrized by

$$\delta k = \frac{K_1 - m\omega^2}{\omega b} \tag{4}$$

and load parametrized by

$$\omega\tau = \omega R_{\mathrm{L}} C. \tag{5}$$

For an anti-phase overlap varying device like ours, parameters of the linear electromechanical two-port model are given by [33]:

$$C = \frac{C_0 + C_{\mathrm{p}} + C_{\mathrm{L}}}{2} \tag{6}$$

$$\Gamma = \frac{C_0 V_{\mathrm{T}}}{x_0} \tag{7}$$

$$K_1 = k_{\mathrm{m}} + \frac{2C_0^2 V_{\mathrm{T}}^2}{x_0^2\big(C_0 + C_{\mathrm{p}} + C_{\mathrm{L}}\big)k_{\mathrm{m}} + 2C_0^2 V_{\mathrm{T}}^2} \tag{8}$$

The short circuit stiffness K_0 and the open-circuit stiffness K_1 are related by $K_0 = (1 - k^2)K_1$, where the coupling factor is given by $k^2 = \frac{\Gamma^2}{K_1 C}$.

The proof mass m, nominal overlap capacitance C_0, mechanical spring stiffness k_{m} are found from the design. Damping coefficient b and the parasitic capacitances C_{p} and C_{L} are estimated based on fitting to values of figure of merit $k^2 Q_{\mathrm{m}} = 4.7$ when $V_{\mathrm{T}} = 47.5$ V.

The analysis of different models of vibro-impact systems was considered by Babitsky and Krupenin [34]. Analytical models approximating purely elastic and inelastic impact

using smooth functions have been reviewed in [35]. The force of interaction has been phenomenologically modeled by different forms based on power laws with or without damping [36]. In real structures, each impact is associated with energy loss and thus the damping should be accounted for in modeling. This damping is in general a nonlinear function of deformation and velocity. In this work, during the contact period, the impact mechanism is modeled as Hertzian contact force affiliated with hysteresis damping, which may then be written in terms of the penetration $\delta = |x| - X_{\max}$ [37] as

$$F_{\mathrm{s}} = k_{\mathrm{s}}\delta^{\frac{3}{2}}\big(1 + \frac{3}{4}\frac{\dot{\delta}}{\dot{\delta}_{-}}\big(1 - e^2\big)\big) \tag{9}$$

where k_{s} is the contact stiffness coefficient and $\dot{\delta}_{-}$ is the velocity difference of the two colliding bodies at the beginning of impact. The coefficient of restitution e is chosen as $e = 0.7$ according to experiments [38]. The contact stiffness can be obtained from an analytical model for impact mechanism between semi cylindrical bumps and flat surfaces [39, 40]. As a simplification of the SPICE simulations, we treat the impact velocity $\dot{\delta}_{-}$ as a constant parameter that is extracted from initial simulations at high acceleration values and without end-stop damping.

The lumped-model allows us to investigate performance of the device in impact regime where the load is optimized at every acceleration amplitude and the driving frequency is kept (fixed) at open-circuit frequency. Load optimization further increases power when $A > A_{\mathrm{c}}$ as shown by the simulation results in figure 9.

The proof-mass displacement $x(t)$ and the mechanical force $F_{\mathrm{m}}(t) = K_1 x(t) - F_{\mathrm{s}}(t)$ are periodic signals with fundamental period T and can be expanded in a Fourier series

$$x\big(t\big) = \sum_{n=-\infty}^{\infty} X_n e^{jn\omega t}, \tag{10}$$

$$F_{\mathrm{m}}\big(t\big) = \sum_{n=-\infty}^{\infty} F_n e^{jn\omega t} \tag{11}$$

where $\omega = 2\pi/T$ is the fundamental angular frequency. The coefficients are

$$X_n = \frac{1}{T}\int_0^T x\big(t\big)e^{-jn\omega t}\,\mathrm{dt}, \tag{12}$$

$$F_n = \frac{1}{T}\int_0^T F_{\mathrm{m}}\big(t\big)e^{-jn\omega t}\,\mathrm{dt}. \tag{13}$$

A meaningful effective stiffness K_{eff} can be obtained by considering the ratio of the fundamental harmonic ($n = 1$) coefficients of the mechanical force and displacement, i.e.

$$K_{\mathrm{eff}} = \mathrm{Re}\left\{\frac{F_1}{X_1}\right\} = \mathrm{Re}\left\{\frac{\int_0^T F_{\mathrm{m}}\big(t\big)e^{-\mathrm{j}\omega\mathrm{t}}dt}{\int_0^T x\big(t\big)e^{-\mathrm{j}\omega\mathrm{t}}dt}\right\} \tag{14}$$

where $x\big(t\big)$ and $F_{\mathrm{m}}\big(t\big)$ signals are extracted from simulation results. Focusing on the first harmonic makes sense because, as observed in [41,42], it can be sufficient to model the harvester accurately. We have checked that at the largest acceleration considered here, the first harmonic accounts for more than 90% of the mean square velocity for $M = 3.2$.

Comparisons of optimum powers along with the variation of stiffness and load are given in figure 9. The results are given on a nondimensional form that is normalized with respect to

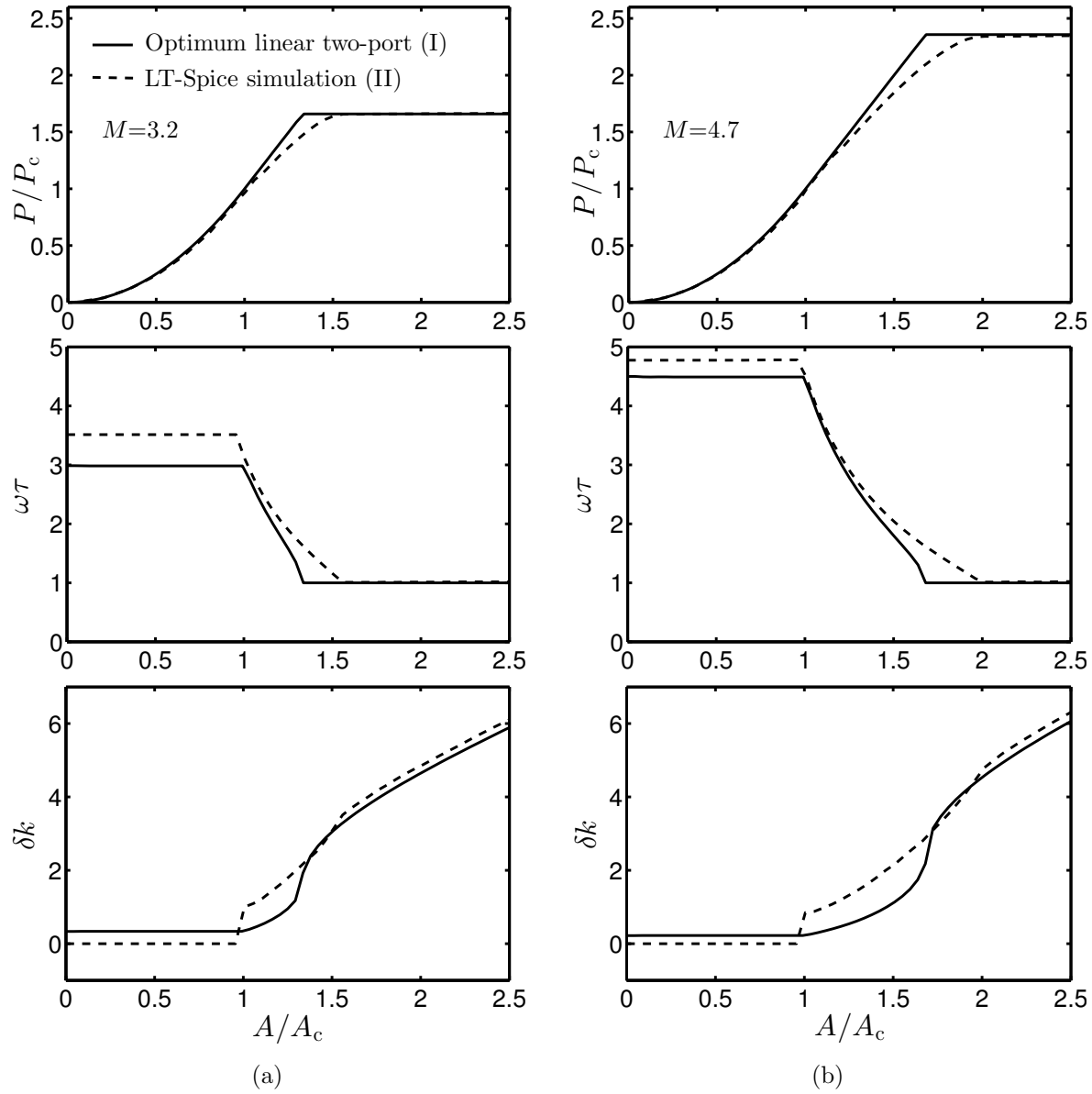

Figure 9: Comparison results between numerically contemporaneous optimization of load and stiffness for displacement-limited linear two-port model without end-stops (solid-lines) and optimal load for lumped-model under the effect of end-stops (dash-line), with different values of figure of merit (a) M=3.2 and (b) M=4.7.

characteristic quantities that can be defined for many harvester architectures. The theoretical optimum normalized power $P/P_{\rm c}$ for the linear device is expressed as a function of the transducer figure of merit M, normalized input acceleration amplitude $A/A_{\rm c}$, parametrized stiffness δk and parametrized load $\omega\tau$. The two cases shown are: (I) Fully analytical solution of the optimal two-port model without end-stops and with displacement constraints enforced be load and stiffness tuning, adapted from [32]. (II) The load optimized two-port model with end-stops obtained by simulations. We substitute K_1 in (4) by $K_{\rm eff}$ when evaluating δk for case (II).

At low accelerations $A < A_{\rm c}$ such that the proof mass motion does not reach the limit, the impact force is absent. Therefore, the effective stiffness is identical to the open-circuit stiffness.

We drove the device at the open-circuit frequency instead of the nearby optimal frequency. The small difference between the optimal stiffness and the open-circuit stiffness is the reason for the different load and stiffness in the two cases. Even so, the output powers obtained are still indistinguishable.

When the drive amplitude is large enough, the proof mass displacement reaches, and is limited to, the maximum amplitude $X_{\max}$. There is a range of acceleration amplitudes in which the optimum power of case (II) is a bit lower than that of case (I) which, as the experiments, closely follows the optimal VDRG before leveling out. That difference can be explained by the imprecision of the vibro-impact force model (9). It was found that the impact damping is highly nonlinear and primarily depends on the type of collision and the excitation levels [36]. The analysis of the complicated response of contact damper is beyond the scope of the present work and is not necessary for our purpose. At large amplitudes of the external acceleration, we observe close agreement between the values of normalized power, $\omega\tau$ and δk for the two cases. This confirms that the rigid end-stops contributes an effective stiffness of the harvester that is close to the optimum value. Hence, stiffness tuning does not need to be made actively as long as one has end-stops and the load is actively tuned.

5. Conclusion

Electrical damping was controlled through load resistance to maximize power for a vibration energy harvester under displacement-constrained operation. In addition the electromechanical coupling was varied. The measured power closely follows the optimal VDRG even between the two extremes of unconstrained proof mass motion only limited by damping and displacement-limited operation with saturated power. The load optimization makes a gradual transition between these two extremes which we can think of respectively as maximum power-transfer and maximum efficiency. For displacement-limited operation, there are significant improvements in power from increasing electromechanical coupling even for a high-coupling device. Qualitatively the results were very similar to an optimal linear two-port which has a displacement limit implemented by load and stiffness tuning. Numerical simulations confirmed that the observed behaviour can be interpreted as the end-stops contributing a tuning of the effective stiffness to a value that is close the optimal stiffness value for the harvester without end-stops. Hence, one can obtain near optimal power without active stiffness tuning if there are end-stops and the load is actively tuned.

Acknowledgment

This work was supported by the Research Council of Norway through Grant no. 229716/E20.

References

[1] Wischke M, Masur M, Krner M and Woias P 2011 Vibration harvesting in traffic tunnels to power wireless sensor nodes *Smart Materials and Structures* **20** 085014

[2] Ylli K, Hoffmann D, Becker P, Willmann A, Folkmer B and Manoli Y 2014 Human motion energy harvesting for aal applications *Journal of Physics: Conference Series* **557** 012024

[3] Lee J, Oh J, Kim H and Choi B 2014 Strain-based piezoelectric energy harvesting for wireless sensor systems in a tire *Journal of Intelligent Material Systems and Structures*

[4] Singh K B, Bedekar V, Taheri S and Priya S 2012 Piezoelectric vibration energy harvesting system with an adaptive frequency tuning mechanism for intelligent tires *Mechatronics* **22** 970 – 988 ISSN 0957-4158

[5] Deterre M, Risquez S, Bouthaud B, Molin R D, Woytasik M and Lefeuvre E 2013 Multilayer out-of-plane overlap electrostatic energy harvesting structure actuated by blood pressure for powering intra-cardiac implants *Journal of Physics: Conference Series* **476** 012039

[6] Mitcheson P D 2010 Energy harvesting for human wearable and implantable bio-sensors *Engineering in Medicine and Biology Society (EMBC), 2010 Annual International Conference of the IEEE* pp 3432–3436 ISSN 1557-170X

[7] Starner T 1996 Human-powered wearable computing *IBM Syst. J.* **35** 618–629 ISSN 0018-8670

[8] Cepnik C, Lausecker R and Wallrabe U 2013 Review on electrodynamic energy harvesters – a classification approach *Micromachines* **4** 168–196 ISSN 2072-666X
[9] Mitcheson P D, Yeatman E M, Rao G K, Holmes A S and Green T C 2008 Energy harvesting from human and machine motion for wireless electronic devices *Proceedings of the IEEE* **96** 1457–1486
[10] Roundy S, Wright P K and Rabaey J 2003 A study of low level vibrations as a power source for wireless sensor nodes *Computer Communications* **26** 1131–1144
[11] Roundy S, Wright P and Rabaey J 2004 *Energy Scavenging for Wireless Sensor Networks: With Special Focus on Vibrations* (Springer US) ISBN 9781402076633
[12] Soliman M S M, Abdel-Rahman E M, El-Saadany E F and Mansour R R 2008 A wideband vibration-based energy harvester *Journal of Micromechanics and Microengineering* **18** 115021 (11pp)
[13] Moss S D, Hart G A, Burke S K and Carman G P 2014 Hybrid rotary-translational vibration energy harvester using cycloidal motion as a mechanical amplifier *Applied Physics Letters* **104** 033506
[14] Gu L and Livermore C 2012 Compact passively self-tuning energy harvesting for rotating applications *Smart Materials and Structures* **21** 015002
[15] Vandewater L A and Moss S D 2013 Probability-of-existence of vibro-impact regimes in a nonlinear vibration energy harvester *Smart Materials and Structures* **22** 094025
[16] Haroun A, Yamada I and Warisawa S 2015 Micro electromagnetic vibration energy harvester based on free/impact motion for low frequencylarge amplitude operation *Sensors and Actuators A: Physical* **224** 87 – 98 ISSN 0924-4247
[17] Hoffmann D, Folkmer B and Manoli Y 2009 Fabrication, characterization and modelling of electrostatic micro-generators *Journal of Micromechanics and Microengineering* **19** 094001 (11pp)
[18] Halvorsen E, Le C P, Mitcheson P D and Yeatman E M 2013 Architecture-independent power bound for vibration energy harvesters *Journal of Physics: Conference Series* **476** 012026
[19] Mitcheson P D, Green T C, Yeatman E M and Holmes A S 2004 Architectures for vibration-driven micropower generators *Journal of Microelectromechanical Systems* **13** 429–440 ISSN 1057-7157
[20] Le C P, Halvorsen E, Srsen O and Yeatman E M 2012 Microscale electrostatic energy harvester using internal impacts *Journal of Intelligent Material Systems and Structures* **23** 1409–1421
[21] Le C P, Halvorsen E, Søråsen O and Yeatman E M 2012 Comparison of transducing end-stops with different stiffness in MEMS electrostatic energy harvesters *Proc. PowerMEMS,* 444447
[22] Truong B D, Le C P and Halvorsen E 2014 Electric control of power extracting end-stop for MEMS vibration energy harvesting *Journal of Physics: Conference Series* **557** 012012
[23] Renaud M, Elfrink R, Jambunathan M, de Nooijer C, Wang Z, Rovers M, Vullers R and van Schaijk R 2012 Optimum power and efficiency of piezoelectric vibration energy harvesters with sinusoidal and random vibrations *Journal of Micromechanics and Microengineering* **22** 105030
[24] Truong B D, Le C P and Halvorsen E 2015 Experiments on power optimization for displacement-constrained operation of a vibration energy harvester *Journal of Physics: Conference Series* **660** 012012
[25] D'hulst R, Sterken T, Puers R, Deconinck G and Driesen J 2010 Power processing circuits for piezoelectric vibration-based energy harvesters *Industrial Electronics, IEEE Transactions on* **57** 4170–4177 ISSN 0278-0046
[26] Blystad L C J, Halvorsen E and Husa S 2010 Piezoelectric mems energy harvesting systems driven by harmonic and random vibrations *IEEE Transactions on Ultrasonics, Ferroelectrics, and Frequency Control* **57** 908–919 ISSN 0885-3010
[27] Le C P and Halvorsen E 2013 Wide tuning-range resonant-frequency control by combining electromechanical softening and hardening springs *Solid-State Sensors, Actuators and Microsystems (TRANSDUCERS EUROSENSORS XXVII), 2013 Transducers Eurosensors XXVII: The 17th International Conference on* pp 1352–1355
[28] Renno J M, Daqaq M F and Inman D J 2009 On the optimal energy harvesting from a vibration source *Journal of Sound and Vibration* **320** 386 – 405 ISSN 0022-460X
[29] Peano F and Tambosso T 2005 Design and optimization of a MEMS electret-based capacitive energy scavenger *Microelectromechanical Systems, Journal of* **14** 429–435 ISSN 1057-7157
[30] Tilmans H A C 1996 Equivalent circuit representation of electromechanical transducers: I. lumped-parameter systems *Journal of Micromechanics and Microengineering* **6** 157
[31] Kaur S, Le C P and Halvorsen E 2016 Optimal operation of two-port energy harvester with power-extracting end-stops *Unpublished*
[32] Halvorsen E 2015 Optimal load and stiffness for displacement-constrained vibration energy harvesters *preprint, arXiv:submit/1500452*
[33] Le C P and Halvorsen E 2012 MEMS electrostatic energy harvesters with end-stop effects *Journal of Micromechanics and Microengineering* **22** 74013–74024
[34] Babitsky V and Krupenin V 2001 *Vibration of Strongly Nonlinear Discontinuous Systems* Engineering online

library (Springer) ISBN 9783540414476
[35] Manevitch L I and Gendelman O V 2008 Oscillatory models of vibro-impact type for essentially non-linear systems *Proceedings of the Institution of Mechanical Engineers, Part C: Journal of Mechanical Engineering Science* **222** 2007–2043
[36] Ibrahim R 2009 *Vibro-Impact Dynamics: Modeling, Mapping and Applications* Lecture Notes in Applied and Computational Mechanics (Springer Berlin Heidelberg) ISBN 9783642002755
[37] Lankarani H M and Nikravesh P E 1994 Continuous contact force models for impact analysis in multibody systems *Nonlinear Dynamics* **5** 193–207 ISSN 1573-269X
[38] Stronge W 2004 *Impact Mechanics* (Cambridge University Press) ISBN 9780521602891
[39] Norden B N 1973 On the compression of a cylinder in contact with a plane surface *Institute for Basic Standards National Bureau of Standards Washington, D. C. 20234* **NBSIR 73-243**
[40] Truong B D, Le C P and Halvorsen E 2015 Experimentally verified model of electrostatic energy harvester with internal impacts *Micro Electro Mechanical Systems (MEMS), 2015 28th IEEE International Conference on* pp 1125–1128
[41] Blokhina E, Galayko D, Basset P and Feely O 2013 Steady-state oscillations in resonant electrostatic vibration energy harvesters *IEEE Transactions on Circuits and Systems I: Regular Papers* **60** 875–884 ISSN 1549-8328
[42] O'Riordan E, Dudka A, Galayko D, Basset P, Feely O and Blokhina E 2015 Capacitive energy conversion with circuits implementing a rectangular charge-voltage cycle part 2: Electromechanical and nonlinear analysis *IEEE Transactions on Circuits and Systems I: Regular Papers* **62** 2664–2673 ISSN 1549-8328